Pitch-Derived Carbon-Coated Hierarchical Porous Microspheres Constituted of Zeolitic Imidazolate Framework-8 Derived Hollow N-doped Carbon Nanocages and Si Nanospheres for High-Performance Li–Ion Battery Anodes

Jae Seob Lee, Geon Hui Oh, Chungyeon Cho, Noeul Kim, Rakesh Saroha, Sang Mun Jeong, Jae-Oh Shim, Dae Soo Jung, Gi Dae Park,* Yun Chan Kang,* Jin-Sung Park,* and Jung Sang Cho*

In this study, an innovative spray-drying-based approach for the design and synthesis of 3D hierarchical porous microspheres comprised of Si nanospheres and zeolitic imidazolate framework-8 (ZIF-8)-derived hollow N-doped carbon nanocages is presented. This sophisticated design of Si-based carbonaceous framework is characterized by the hollow N-doped carbon cages, which can reinforce the electrical conductivity of Si nanosphere, facilitate the electrolyte penetration into the nanostructure, and effectively alleviate the volume changes that occur during cycling. Notably, pitch-derived carbon is coated evenly on the surface of the framework, generating a conformal coating that can effectively encapsulate the Si nanoparticles. The prepared composite microsphere is characterized by the 3D conductive network to which Si nanoparticles are evenly distributed, which play the role of a powerful mixed ion and electron conductor, highly enhancing the electrochemical properties when applied as anodes in lithium–ion batteries. The microspheres exhibit high structural robustness during 500 charge–discharge cycles when cycled at 1.0 A g^{-1}. To validate the practicability, the microspheres are blended with graphite for preparation of anode and coupled with Li(Ni$_{0.8}$Co$_{0.1}$Mn$_{0.1}$)O$_2$ (NCM811) to prepare full cell, which exhibit ≈91% capacity retention after 100 cycles at 0.5 C.

1. Introduction

Although significant progress has been made in the development of other next-generation energy storage systems, lithium–ion batteries (LIBs) remain the dominant energy storage technology.[1–5] To meet the demands of the upcoming electric vehicle era, the development of LIBs with high-energy density is crucial.[1,4–6] While considerable progress has been made on the cathode side, limited innovation has been made on the anode, where graphite with theoretical capacity of 372 mA h g^{-1} remains the standard for commercial LIBs for decades.[1,5,7] In this context, Si has emerged as a highly promising alternative, offering nearly 10 times the theoretical capacity of graphite and a low electrode potential of ≈0.4 V versus Li/Li$^+$, making it an ideal candidate for next-generation anodes.[6,8–11] Despite its high capacity, Si suffers from significant challenges, including large volume expansion during cycling,

J. S. Lee, G. H. Oh, R. Saroha, J. S. Cho
Department of Engineering Chemistry
Chungbuk National University
Chungbuk 28644, Republic of Korea
E-mail: jscho@cbnu.ac.kr

J. S. Lee, N. Kim, Y. C. Kang
Department of Materials Science and Engineering
Korea University
Anam-Dong, Seongbuk-Gu, Seoul 02841, Republic of Korea
E-mail: yckang@korea.ac.kr

C. Cho
Department of Biomedical Materials Science
Jeonbuk Advanced Bio-convergence Academy
Wonkwang University
Iksan, Jeonbuk 54538, Republic of Korea

R. Saroha, J.-S. Park
Department of Materials Science and Engineering
Ajou University
Suwon 16499, Republic of Korea
E-mail: jinsung@ajou.ac.kr

S. M. Jeong
Department of Chemical Engineering
Chungbuk National University
Chungbuk 28644, Republic of Korea

J.-O. Shim
Department of Chemical Engineering/Nanoscale Environmental Sciences and Technology Institute
Wonkwang University
460 Iksan-daero, Iksan-si, Jeollabuk-do 54538, Republic of Korea

which leads to capacity fading and poor cycling stability.[8–12] To address these issues, various strategies have been explored, including the development of advanced nanostructure designs that incorporate carbon composite.[13–15]

Among various carbon materials suitable for compositing with Si, the use of zeolitic imidazolate framework-8 (ZIF-8)-derived nitrogen-doped carbon matrices has garnered significant interest.[16,17] ZIF-8, a typical metal-organic framework, is known for its high surface area, tunable pore structure, and thermal stability, making it an excellent precursor for creating porous carbon-based materials.[18–21] By introducing nitrogen doping into the carbon matrix, additional active sites are created, enhancing the conductivity and improving the electrochemical performance of the material.[16,18] Furthermore, ZIF-8-derived N-doped carbon provides an effective buffer to accommodate the large volume changes of Si during cycling, offering both structural stability and high conductivity.[16,22–24] Chen et al. prepared Si nanoparticles enclosed in a hollow nitrogen-doped carbon layer derived from ZIF-8 for use as anode in LIBs. By simply compositing with ZIF-8 derived carbon, it was demonstrated that the electrochemical stability is enhanced to a large extent in comparison with pristine Si anodes.[25]

Another promising approach to enhancing the electrochemical performance of Si anodes is by compositing them with pitch-derived carbon. One of the primary benefits of pitch-derived carbon coating is its ability to form a highly conductive and flexible layer around the Si particles.[26,27] This conformal coating enhances the electrical conductivity of the anode, which is crucial for improving the overall cycling performance and rate capability.[27,28] The carbon coating also acts as a physical buffer, mitigating the mechanical stresses caused by the large volume expansion and contraction of Si during the charge–discharge cycles.[29,30] In addition, pitch-derived carbon coatings can also enhance the adhesion between Si particles and the conductive network, further improving the battery performance.[31,32] Chae et al. demonstrated that Si particles composited with carbon derived from petroleum pitch exhibited superior
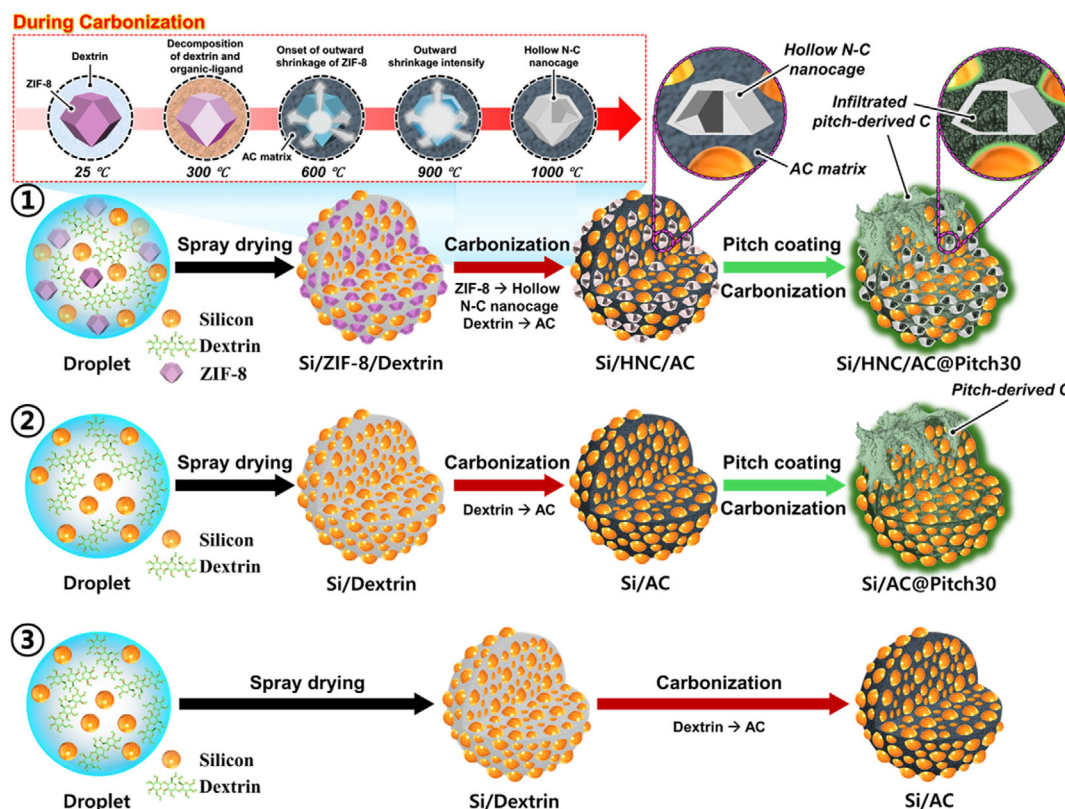
D. S. Jung
Energy Storage Materials Center
Korea Institute of Ceramic Engineering and Technology
Jinju, Gyeongnam 52851, Republic of Korea

G. D. Park
Department of Advanced Materials Engineering
Chungbuk National University
Chungbuk 28644, Republic of Korea
E-mail: gdpark@chungbuk.ac.kr

J.-S. Park
Department of Energy Systems Research
Ajou University
Suwon 16499, Republic of Korea

J. S. Cho
Biomedical Research Institute
Chungbuk National University Hospital
Chungbuk 28644, Republic of Korea

J. S. Cho
Advanced Energy Research Institute
Chungbuk National University
Cheongju, Chungbuk 28644, Republic of Korea

electrochemical performance compared to those prepared using the conventional chemical vapor deposition process.[33]

In this study, we propose a spray-drying-based strategy to fabricate 3D hierarchical porous microspheres composed of Si nanoparticles (50–140 nm in size) and hollow nanocages (HNC) doped with nitrogen derived from ZIF-8 (denoted as Si/HNC/AC microsphere), to which a uniform pitch-derived carbon layer is coated (denoted as Si/HNC/AC@Pitch30 microsphere). Through the spray-drying process, microspheres with a uniform distribution of ZIF-8 and Si nanoparticles can be formed, which is carbonized to yield Si/HNC/AC microspheres composed of evenly distributed Si nanoparticles, nitrogen-doped carbon hollow nanocages, and amorphous carbon (AC). Pitch-derived carbon layer was coated on the surface of HNC building blocks and microsphere, resulting in the formation of Si/HNC/AC@Pitch30 microspheres with high structural stability and improved electrical conductivity. The microspheres, when applied as anode in LIBs, exhibited excellent electrochemical performance, maintaining a discharge capacity of 651 mA h g^{-1} even after 500 cycles at a current density of 1.0 A g^{-1}. The anode was mixed with commercial graphite in a 10:90 weight ratio, and the resulting electrode showed a stable cyclic performance, where 84% of its capacity was maintained after 200 cycles at a current density of 0.5 C (1.0 C = 516 mA g^{-1}). In a full cell performance evaluation combined with a commercial Li(Ni$_{0.8}$Co$_{0.1}$Mn$_{0.1}$)O$_2$ (NCM811) cathode, the cell demonstrated an excellent cycle performance, with a capacity retention rate of 91% after 100 cycles at 0.5 C (1.0 C = 180 mA g^{-1}).

2. Results and Discussion

The schematic illustration of the preparation procedure for Si/HNC/AC@Pitch30, Si/AC@Pitch30, and Si/AC microspheres via spray drying process is provided in **Scheme 1**. To obtain Si/HNC/AC@Pitch30 microspheres, colloidal solution that contains Si nanospheres and dextrin was prepared. Si nanospheres with sizes ranging from 50 to 140 nm have been employed since they form stable colloidal solution and are reported to exhibit the highest electrochemical performance among Si nanoparticles with different sizes.[34] Spray drying of the precursor solution resulted in the formation of microspheres in which Si/ZIF-8/dextrin microspheres are well-dispersed. The setup for the spray drying apparatus is provided in Scheme S1 (Supporting Information). The resultant powder then undergoes carbonization, where the dextrin decomposes and transforms into AC and dense ZIF-8 particles transform into N-doped carbon nanocages with central mesopores. It has been reported that outward shrinkage of ZIF-8 particle occurs during the carbonization process when ZIF-8 particles are enclosed by carbon or polymer sources, resulting in the formation of hollow carbon nanocages.[35–37] During the carbonization process, Zn component from ZIF-8 particles is converted into Zn metal and evaporated due to the high temperature annealing process.[38–40] Simple spray drying process and one-step carbonization yielded Si/HNC/AC microspheres, which is characterized by the 3D framework consisted of evenly distributed Si nanospheres. Si nanoparticles are composited with hollow N-doped carbon and AC which can supplement the electrical conductivity

Scheme 1. Schematic representation of formation mechanism of ① pitch-derived carbon coated 3D hierarchical porous microspheres composed of silicon nanoparticles and hollow nanocages doped with nitrogen derived from ZIF-8 (Si/HNC/AC@Pitch30 microsphere), ② pitch-derived carbon coated microspheres composed of silicon nanoparticles and AC (Si/AC@Pitch30 microsphere), and ③ Si/AC composite microspheres.

by forming a 3D conductive matrix. In order to reinforce structural integrity as well as provide additional electrical conductivity, pitch-derived carbon coating is introduced to the surface and the interior of Si/HNC/AC by utilizing pitch-dissolved tetrahydrofuran (THF) solution that can be infiltrated in the porous microspheres. Carbonization of the mixture of Si/HNC/AC and pitch carbon results in the formation of Si/HNC/AC@Pitch30 microspheres, where the optimized amount of pitch determined from empirical experiments is 30 wt%. To demonstrate the effect of HNC distributed within the 3D matrix, Si/AC@Pitch30 microspheres were prepared from the identical method, with the exception that ZIF-8 is not included in the spray drying solution. Furthermore, to evaluate the effect of pitch-derived carbon coating, Si/AC microspheres were obtained by spray drying of solution that contains Si nanoparticles and dextrin and subsequent carbonization process. The amount of dextrin added to the spray solution was different for the preparation of each microsphere to make sure the final carbon content in the microspheres is constant.

The morphological and crystallographic characteristics of Si/HNC/AC microspheres prepared from spray drying process and subsequent carbonization heat treatment at 1000 °C for 2 h under a nitrogen atmosphere are provided in **Figure 1**. Field emission scanning electron microscopy (FE-SEM) images and the X-ray diffraction (XRD) patterns of Si nanoparticles and ZIF-8 particles used for spray drying are shown in Figure S1

(Supporting Information), where the sizes of the particles were determined to be 50–140 nm and 40–50 nm, respectively. FE-SEM images of Si/ZIF-8/dextrin microspheres obtained directly from spray drying process revealed independent 3D microspheres with no aggregation between the particles (Figure S2a, Supporting Information). Tiny Si and ZIF-8 building blocks that constitute the microspherical superstructure can be observed in Figure S2b (Supporting Information). XRD pattern of the microsphere revealed distinct peaks corresponding to Si and ZIF-8 phases, which is inherited from the particles used to form colloidal spray drying solution (Figure S2c, Supporting Information). Thermogravimetric analysis (TGA) curves of Si/ZIF-8/dextrin microspheres and ZIF-8 particles were obtained in a temperature range of 25–1200 °C under N_2 atmosphere (Figure S3, Supporting Information). For Si/ZIF-8/dextrin microspheres (Figure S3a, Supporting Information), an initial weight loss below 200 °C was observed, which is attributed to the removal of adsorbed water molecules in the microsphere. A significant weight loss between 200 and 300 °C corresponds to the decomposition of dextrin.[41] Beyond 300 °C, both Si/ZIF-8/dextrin microspheres and ZIF-8 polyhedra show a gradual decrease in weight due to the collapse of the ZIF-8 framework and the breakdown of organic linkers. Notably, for ZIF-8 polyhedra (Figure S3b, Supporting Information), an additional weight loss with a distinct slope at temperatures higher than 900 °C indicates the evaporation of Zn metal, consistent with its known
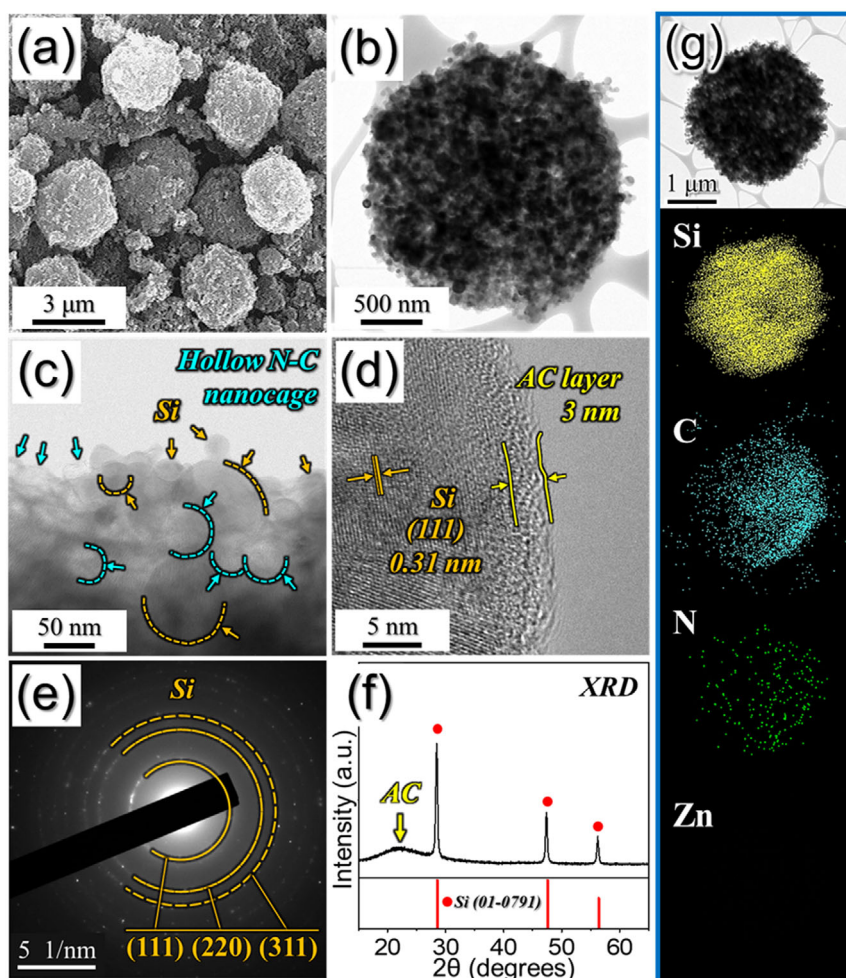
Figure 1. Physical characterizations of Si/HNC/AC microsphere obtained by spray drying and subsequent carbonization at 1000 °C: a) FE-SEM image, b,c) TEM images, d) HR-TEM image, e) SAED pattern, f) XRD pattern, and g) elemental dot mapping images.

boiling point of ≈907 °C.[38–40] FE-SEM image in Figure 1a reveals that even after high-temperature carbonization, the spherical feature is maintained, and Si/HNC/AC microspheres with an average size of ≈3 μm were synthesized. Transmission electron microscopy (TEM) image of the microsphere clearly reveals that spherical Si nanoparticles, with sizes ranging from 50 to 140 nm, are well-dispersed in the 3D HNC/AC matrix (Figure 1b). The co-existence of Si nanoparticles and hollow N-doped C nanocages could be confirmed in the magnified TEM images (Figure 1c). ZIF-8 particles were embedded in the carbonaceous matrix originating from dextrin, which resulted in the outward shrinkage of ZIF-8 during thermal treatment, resulting in the formation of HNC nanocages. The high-resolution TEM (HR-TEM) image in Figure 1d shows that the dextrin used as the carbon precursor formed an AC layer on the surface of Si nanoparticles after the high-temperature heat treatment, and its thickness was confirmed to be 3 nm. The HR-TEM image revealed lattice fringes separated by 0.31 nm, which correspond to the (111) plane of Si. The selected area electron diffraction (SAED) pattern shown in Figure 1e displays three diffraction rings due to the presence of Si within the structure.

The XRD pattern in Figure 1f reveals a broad peak caused by the AC derived from N-doped C nanocages and dextrin, as well as three distinct peaks corresponding to the Si nanoparticles. The elemental mapping image shown in Figure 1g indicates that Si nanoparticles and nitrogen (N)-doped carbon (C) are uniformly distributed within the microspheres. Zn element was not found in the microsphere, suggesting that Zn ions evaporated during the high-temperature heat treatment process.

To improve the structural robustness and achieve optimized electrochemical performance, both the interior and the outer surface of Si/HNC/AC microspheres were coated by utilizing pitch-containing THF solution and subsequently heat-treated to yield Si/HNC/AC@Pitch microspheres (**Figure 2**). Si/HNC/AC microspheres were coated with pitch-derived carbon in different weight percentages (10, 20, 30, 40, and 50 wt%), labeled as @Pitch 10 wt%, @Pitch 20 wt%, @Pitch 30 wt%, @Pitch 40 wt%, and @Pitch 50 wt%, respectively. The morphology of Si/HNC/AC microspheres without pitch coating and with different amounts of pitch carbon is shown in Figure 2a–f. As the amount of pitch for coating Si/HNC/AC microspheres increased, it was observed that pitch-derived carbon was coated
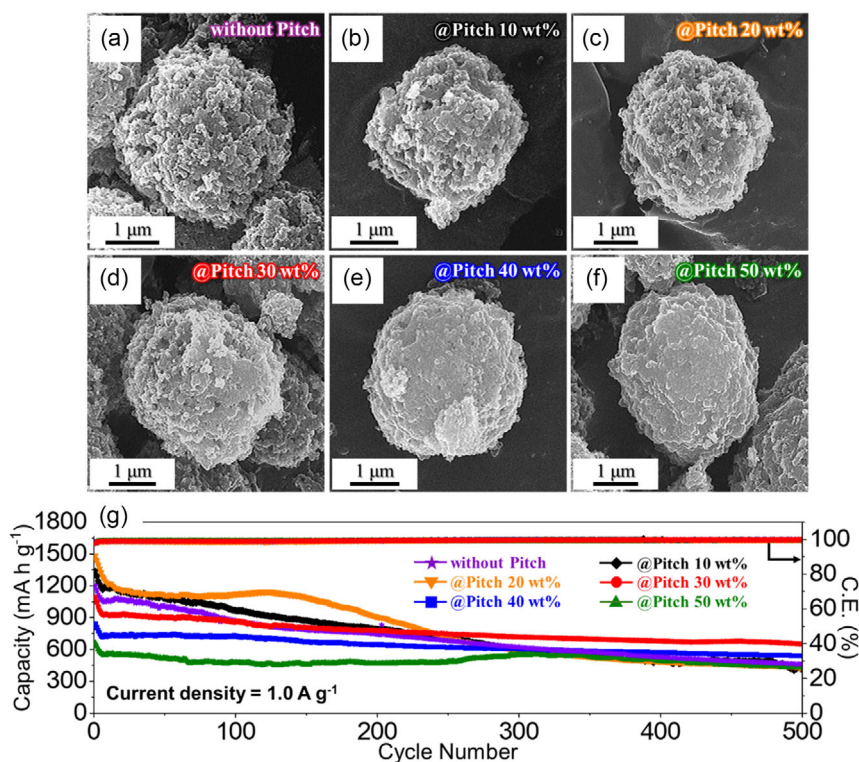
**ADVANCED
SCIENCE NEWS**

www.advancedsciencenews.com

**small
structures**

www.small-structures.com

Figure 2. a–f) FE-SEM images and g) cycling performance of Si/HNC/AC and Si/HNC/AC@Pitch microspheres coated with different amounts of pitch powder at a current density of 1.0 A g^{-1}; a) without pitch, b) 10 wt%, c) 20 wt%, d) 30 wt%, e) 40 wt%, and f) 50 wt%.

more densely and thickly on both the surface and inside of the Si/HNC/AC nanostructure. The carbon content in each sample was determined from elemental analysis (EA) analysis, which clearly showed a trend of increasing carbon content as the amount of pitch-derived carbon used for coating increased, as shown in Table S1 (Supporting Information). The nitrogen content in the microspheres was similar ($\approx$2 wt%) where there was only a slight decrease in the nitrogen content even when the amount of pitch for coating Si/HNC/AC microspheres increased. To investigate the impact of pitch-derived carbon coating layers on the cycle performance and to determine the optimum amount of pitch that yield the best electrochemical performance, cycle performance of Si/HNC/AC microspheres with various amount of pitch coating was tested at 1.0 A g^{-1} (Figure 2g). Specific capacity of the six different anodes exhibited a volcano plot as a function of pitch carbon coating amount. A rise in capacity could be observed with the increase as the pitch carbon coating increased up to 20 wt%, followed by a gradual decrease at higher pitch carbon contents (>30 wt%). The increase in capacity could be attributed to the formation of 3D interconnected carbon network derived from pitch carbon with high conductivity. However, as the amount of carbon with relatively lower specific capacity increased, the capacity of pitch carbon-coated Si/HNC/AC microspheres decreased. Si/HNC/AC microspheres without pitch and @Pitch 10 wt% and @Pitch 20 wt% anodes could not withstand the repeated volume expansion of Si nanoparticles and showed rapid capacity decay. Si/HNC/AC microspheres with 20 wt% pitch coating exhibited

an increase in capacity before the capacity decay began. This can be interpreted as the result of Si nanoparticles undergoing volume expansion during repeated charge–discharge cycles, which formed new active interfaces throughout the structure. These interfaces facilitated additional reactions with lithium, causing a temporary increase in capacity. The microspheres with a higher pitch coating content demonstrated much more stable cycle performance, though they showed lower discharge capacities due to higher carbon content in the structure. 30 wt% pitch carbon coating was selected as the optimum coating amount since the anode could secure both high capacity as well as good capacity retention.

To deeply understand the material characteristics of Si/HNC/AC@Pitch30 microspheres, various analytical methods have been adopted and presented in **Figure 3**. FE-SEM image of Si/HNC/AC@Pitch30 microspheres in Figure 3a reveals that the microspheres exhibit independent 3D microspherical morphologies. TEM image of a single microsphere shown in Figure 3b reveals darker morphology in comparison to Si/HNC/AC microspheres (Figure 1b) which exhibit a lighter and more textured appearance, indicative of the pitch carbon layer coated both at the interior and the exterior of the microspheres. High-magnification TEM image of Si/HNC/AC@Pitch30 microspheres (Figure 3c) reveals evenly distributed nanosized Si building blocks that constitute the microsphere. HR-TEM image of the microsphere in Figure 3d reveals pitch-derived carbon layer with average thickness of 1.8 nm coated on the surface of AC layer derived from dextrin with thickness
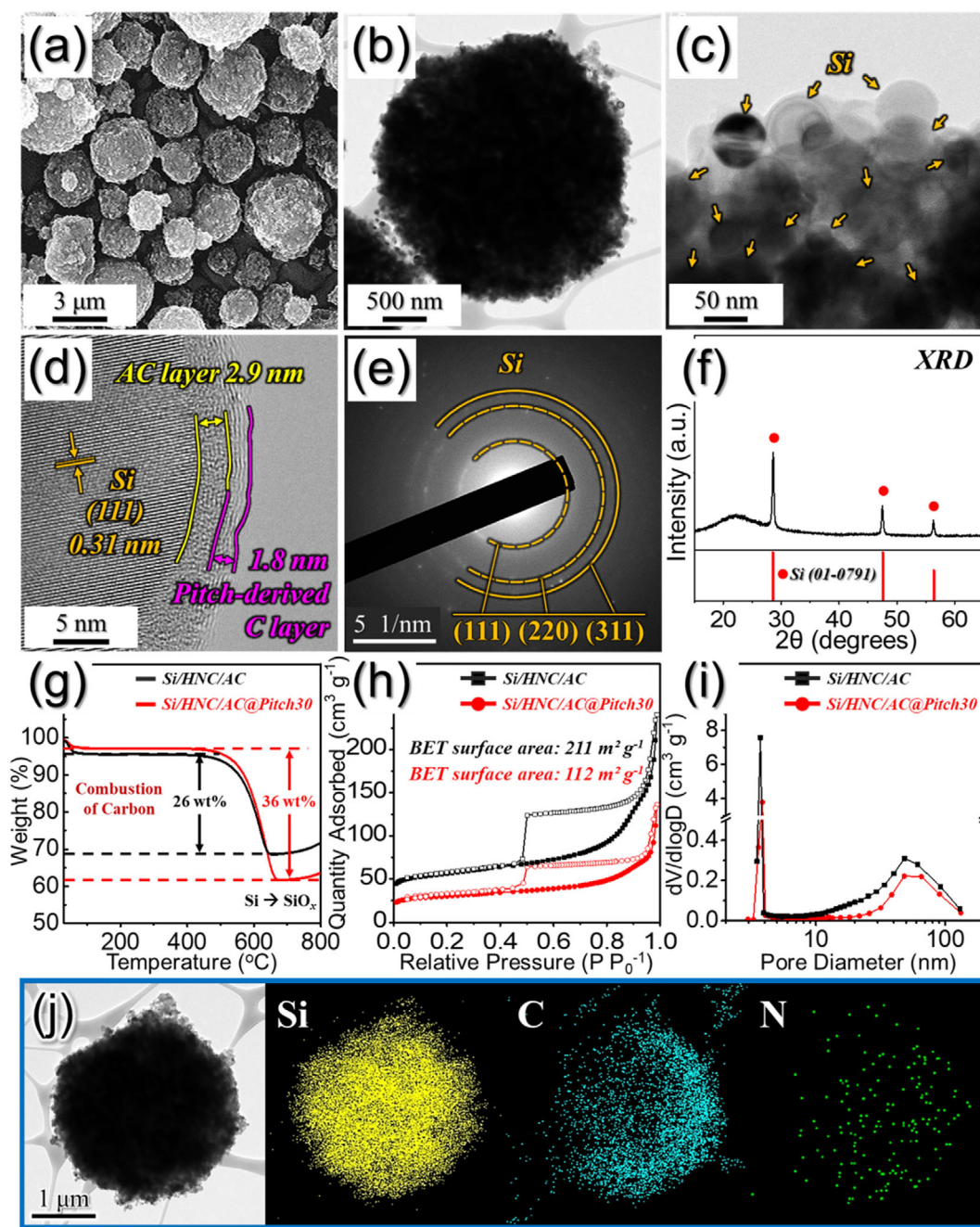
Figure 3. Physical characterizations of Si/HNC/AC@Pitch30 microspheres: a) FE-SEM image, b,c) TEM images, d) HR-TEM image, e) SAED pattern, f) XRD pattern, g) TG curves, h) N$_2$ adsorption–desorption isotherms, i) BJH pore size distributions, and j) elemental dot mapping images.

of 2.9 nm, which completely encapsulates the Si nanoparticles with interlayer spacing of 0.31 nm corresponding to the (111) plane of Si. The SAED pattern of the microsphere reveals three rings corresponding to (111), (220), and (311) planes of Si (Figure 3e). XRD pattern in Figure 3f reveals distinct peaks corresponding to Si (JCPDS card #01-0791). To determine the carbon content in Si/HNC/AC and Si/HNC/AC@Pitch30 microspheres, TGA analysis was conducted under air (Figure 3g). The weight loss that occurs in the temperature

ranging from 500 to 650 °C corresponds to the combustion of carbon. As indicated in the TGA curves, Si/HNC/AC and Si/HNC/AC@Pitch30 microspheres exhibited weight loss of 26 and 36 wt%, respectively, which correspond to the carbon content in each sample. The results are in good match with the carbon content of the microspheres (25.8 and 36.4 wt%) determined from EA (Table S1, Supporting Information). The N$_2$ adsorption–desorption isotherms of Si/HNC/AC and Si/HNC/AC@Pitch30 microspheres (Figure 3h) display type IV isotherms with a distinct

broad hysteresis loop observed within the pressure range of 0.0–1.0 P/P$_0$. The specific surface area of Si/HNC/AC microspheres was as high as 211 m^2 g^{-1}, which can be attributed to the numerous mesopores originating from the central void space of HNCs. After forming a pitch-derived carbon coating at the interior and on the surface of the microsphere, the hysteresis became less distinct and the specific surfaces are decreased to 112 m^2 g^{-1}. The Barrett-Joyner-Halenda (BJH) pore size distribution in Figure 3i confirms the presence of both micro- and mesopores, with peaks at 3.7 and 49.2 nm, respectively. The micropores originate from the AC produced during the carbonization of dextrin and the carbon shells of HNCs. The elemental mapping images in Figure 3j reveals that Si particles are well-distributed within the 3D carbonaceous matrix. Nitrogen was derived from the N-doped carbon obtained from carbonization of ZIF-8. The Raman spectra reveal distinct peaks at ≈514 cm^{-1} corresponding to Si–Si vibrations,[31,42] as well as D- and G-bands at 1351 and 1593 cm^{-1} indicative of carbon structures (Figure S4, Supporting Information). The intensity ratio of I_D/I_G provides a measure of structural disorder in the 3D carbon matrix. After coating with pitch-derived carbon, I_D/I_G value of Si/HNC/AC decreased from 1.01 to 0.99, which indicates a reduction in structural disorder and an increase in graphitization due to pitch treatment.[31,43] To investigate the chemical composition and bonding states of Si/HNC/AC@Pitch30 microspheres, X-ray photoelectron spectroscopy (XPS) analysis was performed (**Figure 4**). The survey spectrum (Figure 4a) reveals the presence of O 1s, N 1s, C 1s, and Si 2p peaks, confirming the incorporation of Si and nitrogen into the carbon framework. The Si 2p spectrum (Figure 4b) shows two characteristic peaks at 99.7 and 100.2 eV, corresponding to Si^0 2p$_{3/2}$ and Si^0 2p$_{1/2}$, respectively.[44] In addition, the peak that occurs at higher binding energy could be deconvoluted into four curves centered at 101.9, 102.8, 103.7, and 104.6 eV,

corresponding to Si^{1+}, Si^{2+}, Si^{3+}, and Si^{4+}, respectively.[45] The deconvolution of the C 1s spectrum (Figure 4c) reveals multiple components, indicating the presence of various carbon bonding. Peaks at 284.6, 285.5, 287.6, and 289.2 eV can be assigned to C=C, C–C/C–N, C=O, and O–C=O bonds, respectively, where the presence of C–N bonding confirms the successful doping of N element in carbon.[46,47] The N 1s spectrum (Figure 1d) further demonstrates the successful doping of nitrogen into the carbon matrix. Deconvolution yields four distinct peaks at 398.5, 400.8, 402.4, and 405.0 eV, attributed to pyridinic-N (N-6), pyrrolic-N (N-5), graphitic-N (N-Q), and oxidized-N (N-X) respectively.[47,48]

To investigate the effect of HNCs derived from ZIF-8 and pitch derived carbon coating on the electrochemical performance, Si/AC and Si/AC@Pitch30 microspheres were prepared. For the synthesis, spray drying solution that contains Si nanoparticles and dextrin was spray dried and carbonized under N$_2$ atmosphere to obtain Si/AC microspheres. Pitch carbon was coated onto the microsphere using the same procedure to obtain Si/AC@Pitch30 microspheres. Here, to compensate for the absence of HNCs and/or pitch-derived carbon in the matrix, the amount of dextrin in the spray drying solution was controlled. The morphological evolution during the preparation was investigated with FE-SEM imaging and shown in Figure S5 (Supporting Information). The morphologies and the material characterization of Si/AC and Si/AC@Pitch30 microspheres are provided in Figure S6 and S7 (Supporting Information), respectively. The FE-SEM image of Si/dextrin microspheres obtained after spray drying in Figure S6a (Supporting Information) reveals that Si nanoparticles are completely encapsulated by the dextrin matrix. After carbonization heat treatment, thermal contraction of carbonaceous matrix occurred during the transformation from dextrin to carbon, resulting in independent particulate morphology that constitute the superstructure (Figure S6b, Supporting Information). TEM image in Figure S6c (Supporting Information) reveals a highly dense microsphere that comprises Si and carbon derived from dextrin. Magnified TEM image shown in Figure S6d (Supporting Information) reveals uniformly distributed Si nanoparticles inside the 3D carbonaceous matrix. The presence of Si nanoparticles could be confirmed from the HR-TEM image and XRD pattern (Figure S6e,f, Supporting Information), and the successful encapsulation of particles by AC layer with thickness of 3.1 nm was ascertained. Pore size analysis shown in Figure S6g,h (Supporting Information) revealed very small hysteresis, indicating that the pores in Si/AC microspheres are mainly constituted of micropores originating from carbonization of dextrin. The even distribution of Si nanoparticles inside a single carbonaceous microsphere could be confirmed from the elemental dot mapping (Figure S6i, Supporting Information). After pitch-derived carbon coating, FE-SEM images of Si/AC@Pitch30 microspheres (Figure S7c, Supporting Information) reveal that the pores between each Si nanoparticle were filled and formed smoother and dense micromorphology. From the HR-TEM image (Figure S7f, Supporting Information), it can be observed that pitch-derived carbon layer is coated on the surface of AC layer, which encapsulate Si nanoparticles. Specific surface areas of Si/AC microspheres and Si/AC@Pitch30 microspheres were 242 to 60 m^2 g^{-1}, respectively, implying that the pitch-derived carbon coating on the surface reduced the pores inside the
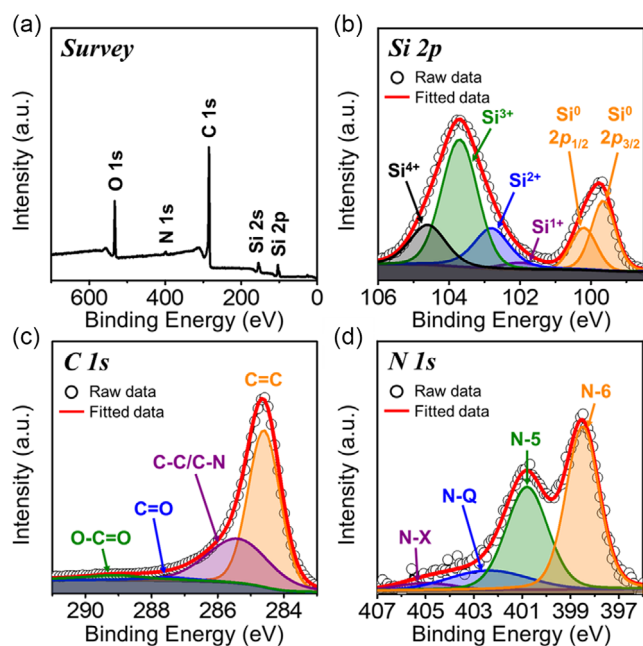

Figure 4. a) XPS survey spectrum, b) Si 2p, c) C 1s, and d) N 1s XPS spectrum of Si/HNC/AC@Pitch30 microsphere.

superstructure (Figure S7h,i, Supporting Information). TGA analysis of Si/AC and Si/AC@Pitch30 microspheres was performed under inert atmosphere to confirm the carbon content in each sample (Figure S8, Supporting Information). Based on weight loss, the carbon content of both microspheres was determined as 32 wt%, which is almost the same as the carbon content obtained from EA results (Table S2, Supporting Information). The nitrogen content of the two microspheres was smaller than that of Si/HNC/AC@Pitch30 microspheres due to the absence of N-doped carbon derived from ZIF-8.

The cyclic voltammetry (CV) curves for Si/HNC/AC@Pitch30, Si/AC@Pitch30, and Si/AC microspheres were obtained within a voltage range of 0.001–1.5 V at a scan rate of 0.1 mV s^{-1} over the first five cycles (**Figure 5**a and S9, Supporting Information). During the initial cathodic scan, broad peaks were observed, corresponding to the formation of the solid electrolyte interphase (SEI) layer; these peaks were not present in subsequent cycles.[49] In the cathodic sweep below 0.3 V, prominent peaks appeared due to the alloying reaction between lithium and Si, resulting in the formation of lithium silicide (Li$_x$Si).[50,51] In the initial anodic scan, two major peaks at 0.34 and 0.51 V were identified, associated with the stepwise delithiation of Li$_x$Si and formation of Si.[51,52] In subsequent cycles, the cathodic sweep displayed dominant peaks at 0.15 V and near 0 V, indicative of the progressive increase in x value within Li$_x$Si.[51,52]

Similarly, anodic peaks continued to appear at 0.35 and 0.52 V, consistent with the CV curves of initial cycle.[52–54] The intensification of both anodic and cathodic peaks after the initial cycle suggests the gradual activation of the Si materials in the anode during repeated charge and discharge processes.[55,56] The initial discharge/charge curves of the microspheres measured at a current density of 0.1 A g^{-1} are presented in Figure 5b. During the initial discharge process, a gradual increase in capacity was observed starting around 1.1 V, which can be attributed to the formation of the SEI layer on the anode surface. Long plateaus appeared below 0.1 V, which can be attributed to the lithiation of Si and the formation of Li$_x$Si. In the charging process, plateau between 0.3 and 0.55 V indicated the delithiation of Li$_x$Si back into Si. These discharge/charge features were consistent with the peaks observed in the CV curves. The initial discharge/charge capacities at 0.1 A g^{-1} were 2200/1589 mA h g^{-1} for Si/HNC/AC@Pitch30 microspheres, 2376/1809 mA h g^{-1} for Si/AC@Pitch30 microspheres, and 2433/1700 mA h g^{-1} for Si/AC microspheres, and their initial Coulombic efficiency values were 72.3, 76.1, and 69.9%, respectively. The lower initial Coulombic efficiency of Si/HNC/AC@Pitch30 microspheres compared to Si/AC@Pitch30 microspheres may be relevant to differences in the specific surface area of the structures. A porous structure with a larger specific surface area increases the contact area with the
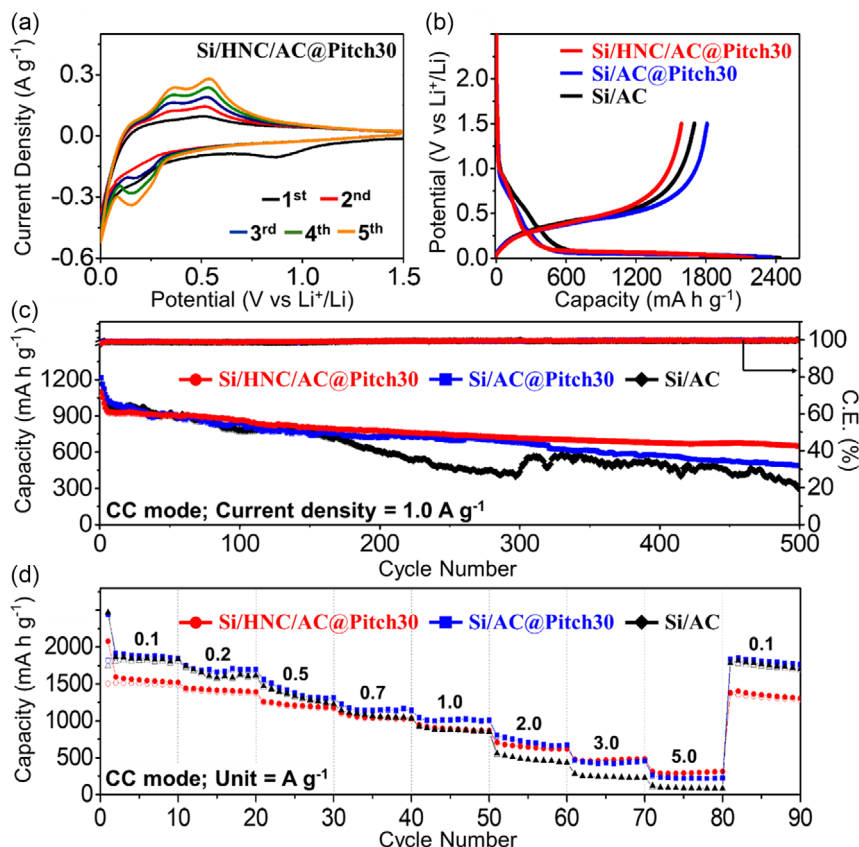

Figure 5. a) CV curves of Si/HNC/AC@Pitch30 microspheres, and b–d) electrochemical properties of Si/HNC/AC@Pitch30, Si/AC@Pitch30, and Si/AC microspheres under CC mode: b) initial Galvanostatic discharge/charge curves at a current density of 0.1 A g^{-1}, c) cycling performance at 1.0 A g^{-1}, and d) rate performance.

ADVANCED
SCIENCE NEWS
www.advancedsciencenews.com

small
structures
www.small-structures.com

electrolyte, leading to higher degree of SEI formation. The SEI forms through irreversible reactions between lithium–ions and the electrolyte, consuming lithium–ions in the process and consequently leading to a lower initial Coulombic efficiency.[57–59] Therefore, Si/HNC/AC@Pitch30 microspheres with a relatively larger specific surface area compared to Si/AC@Pitch30 microspheres exhibit lower initial Coulombic efficiency. To further understand the relationship between pore structure and electrochemical performance, a comparative analysis of the initial Coulombic efficiencies was conducted for Si/HNC/AC and Si/HNC/AC@Pitch microspheres coated with different amounts of pitch-derived carbon (10, 20, and 30 wt%). The initial Coulombic efficiencies increased from 63.1% (uncoated) to 68.5, 69.2, and 72.3%, respectively, as the amount of pitch coating increased (Figure S10, Supporting Information). A decrease in Brunauer-Emmett-Teller (BET) surface area from 211 to 112 m^2 g^{-1} (Figure 3h) has been observed after pitch-derived carbon coating, indicating that pitch infiltration densifies the structure by partially filling the pores. BJH pore size distribution results (Figure 3i) revealed a substantial decrease of ≈50% in the intensity of the ≈3.7 nm peak and a moderate reduction of around 27.5% in the ≈49 nm peak, indicating that micropores were more significantly affected by pitch coating compared to mesopores. It is generally understood that micropores (≈2 nm) offer high surface area but can trap alkali ions, promote side reactions, and thus reduce lower initial Coulombic efficiency.[60] In contrast, mesopores (<50 nm) enhance electrolyte infiltration and lithium–ion transport, contributing to rate capability and cycling stability. Therefore, the improved initial Coulombic efficiency after pitch coating can be primarily attributed to the reduction of micropores and the resulting suppression of side reactions, while the preserved mesoporous structure maintains favorable ion transport pathways essential for long-term stability. The long-term cycle performances of Si/HNC/AC@Pitch30, Si/AC@Pitch30, and Si/AC microspheres were tested at 1.0 A g^{-1} (Figure 5c). For gradual activation of the electrode materials, the current density was changed from 0.1 A g^{-1} (first cycle), 0.5 A g^{-1} (second and third cycle), and to 1.0 A g^{-1} for the rest of the cycles. The discharge capacities of the Si/HNC/AC@Pitch30, Si/AC@Pitch30, and Si/AC microspheres after 500 cycles were 651, 486, and 293 mA h g^{-1}, respectively. Si/HNC/AC@Pitch30 microspheres exhibited the most outstanding cycle life performance among the three anodes, with an average capacity fading rate of 0.06% per cycle. These results demonstrate that the pitch-derived carbon layer and N-doped carbon nanocages can effectively mitigate the volume expansion and structural collapse of Si nanoparticles during repeated charge and discharge processes. The effect of pitch carbon on providing the structural reinforcement for alleviating the volume changes could be demonstrated from comparison of the electrochemical performance of Si/AC@Pitch30 and Si/AC microspheres. To confirm the structural advantages of Si/HNC/AC@Pitch30 microspheres at high charging/discharging rates, the rate capability of the anode was tested along with the control samples, as shown in Figure 5d. Si/HNC/AC@Pitch30 anode exhibited reversible discharge capacities of 1521, 1394, 1178, 1034, 870, 622, 485, and 315 mA h g^{-1} at current densities of 0.1, 0.2, 0.5, 0.7, 1.0, 2.0, 3.0, and 5.0 A g^{-1}, respectively. The capacities of Si/AC@Pitch30 and Si/AC

microspheres decreased from 1847 to 226 mA h g^{-1} and 1835 to 82 mA h g^{-1}, respectively, when the current densities increased from 0.1 to 5.0 A g^{-1}. Si/HNC/AC@Pitch30 microspheres demonstrated the smallest capacity fading among the three anodes, even under high charge/discharge rates, and exhibited excellent rate performance. This result can be attributed to the presence of a highly conductive pitch-derived carbon layer and the nitrogen-doped carbon derived from ZIF-8 material, which altogether formed highly conductive carbonaceous matrix that provided high electrical conductivity to the uniformly distributed Si nanoparticles. The electrochemical properties of the previously reported Si-based anodes for LIBs can be found in Table S3 (Supporting Information), where Si/HNC/AC@Pitch30 microspheres exhibited superior battery performance due to its unique structural advantages.

To evaluate the practical applicability of Si/HNC/AC@Pitch30 microspheres, a full-cell electrochemical test was conducted using the prepared Si-based anode coupled with Li(Ni$_{0.8}$Co$_{0.1}$Mn$_{0.1}$)O$_2$ (NCM811) cathode. Prior to full-cell assembly, Si/HNC/AC@Pitch30 microspheres were mixed with commercial graphite in a ratio of 10:90 (w/w) reflecting the blend ratio typically adopted in third-generation electric vehicles. The FE-SEM image, XRD pattern, and electrochemical performance of the commercial graphite used for the blending are presented in Figure S11 (Supporting Information). Before blending, the standalone cycle performance of Si/HNC/AC@Pitch30 microspheres was assessed under constant current–constant voltage (CC–CV) mode at current densities of 1.0, 3.0, and 5.0 A g^{-1}, demonstrating high capacity retention even after 200 cycles at fast charging/discharging speed (**Figure 6**a). When blended with commercial graphite, the anode delivered a discharge capacity of 449 mA h g^{-1} for the third cycle at 0.5 C (1.0 C = 516 mA g^{-1}), significantly surpassing the capacity (303 mA h g^{-1}) achieved by commercial graphite alone (Figure S11c, Supporting Information). After 200 cycles at 0.5 C, the blended anode retained a reversible capacity of 376 mA h g^{-1}, which is 18% higher than the commercial graphite. Furthermore, as can be seen in Figure 6c, the blended anode also consistently outperformed commercial graphite across various current densities even at a current density of 2.0 C, demonstrating the viability of the prepared Si-based carbonaceous composite as promising anode for electric vehicles. On the cathode side, preliminary evaluations of physical and electrochemical properties for NCM811 particles were performed before integration into the full cell. FE-SEM images revealed the non-aggregated spherical morphology of NCM811 microspheres (Figure S12a,b, Supporting Information) with rhombohedral crystal structure ascertained from XRD pattern in Figure S12c (Supporting Information). The half-cell cycle performance of NCM811 cathode microspheres was tested within a voltage range of 2.7–4.3 V, as shown in Figure S12d (Supporting Information), where discharge capacity of 145 mA h g^{-1} could be delivered after 300 cycles at 0.5 C (1.0 C = 180 mA g^{-1}). The rate performance of NCM811 cathode microspheres was tested, where discharge capacity of 204 mA h g^{-1} is observed at 0.1 C, which is dropped to 59 mA h g^{-1} at 5.0 C. The prepared blended anode was coupled with NCM811 cathode for the assembly of full cells (**Figure 7**a), and the electrochemical performance of the cells within a voltage range between 2.5 and 4.2 V was evaluated. Upon charging to

ADVANCED
SCIENCE NEWS

www.advancedsciencenews.com
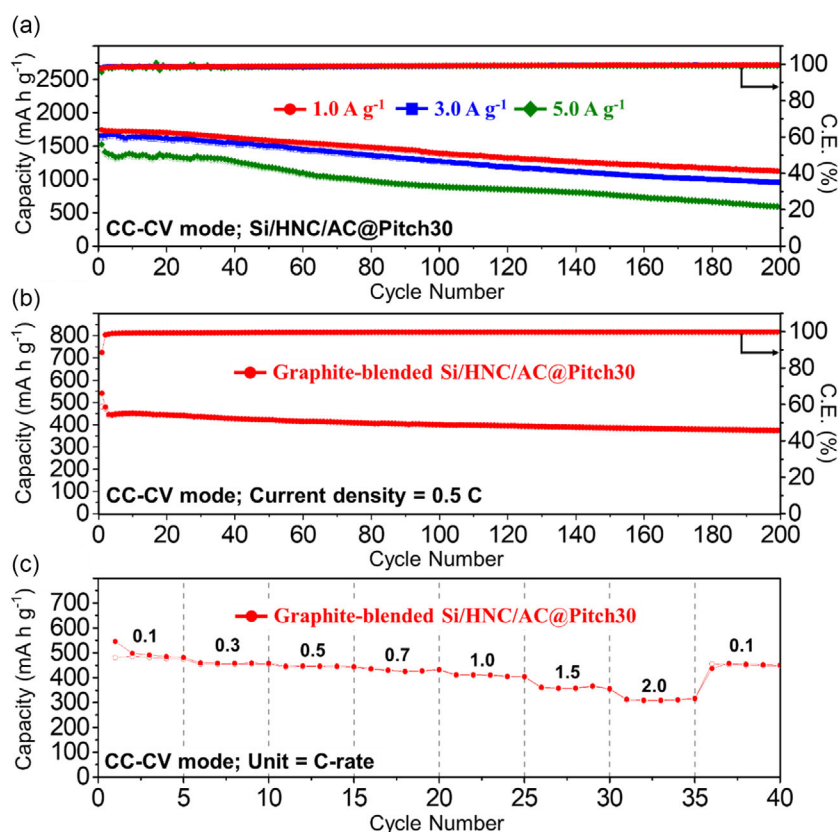
small
structures

www.small-structures.com

Figure 6. Electrochemical properties of Si/HNC/AC@Pitch30 anodes under CC–CV mode: a) cycling performance at current densities of 1.0, 3.0, and 5.0 A g^{-1}; b) cycling performance of graphite-blended Si/HNC/AC@Pitch30 at 0.5 C (1.0 C = 516 mA g^{-1}); and c) rate performance of graphite-blended Si/HNC/AC@Pitch30.

4.2 V at 0.1 C, the cell successfully powered a 5 V, 10 mW LED, which successfully visualized its energy storage capability (Figure 7b). The initial charge and discharge profile for the NCM811∥graphite-Si/HNC/AC@Pitch30 full cell at 0.1 C is provided in Figure 7c, where the full cell exhibited charge/discharge capacities of 219 and 196 mA h g^{-1}. Upon changing the current density of 0.5 C, the full cell exhibited a reversible capacity of 172 mA h g^{-1}. To test the cycle performance, the full cell that adopts anode and cathode loading masses sets at ≈2.21 and 4.21 mg cm^{-2}, respectively, with an N/P ratio of 1.13. After 100 cycles at 0.5 C, the full cell retained a discharge capacity of 164 mA h g^{-1} with ≈91% capacity retention and a high Coulombic efficiency of 99.8%, confirming the robustness and reliability of the Si/HNC/AC@Pitch30 microspheres mixed with commercial graphite (Figure 7d). The reason for the high cyclic stability was unveiled by directly observing the thickness of graphite blended Si/HNC/AC@Pitch30, Si/AC@Pitch30, Si/AC, and Si anodes with the cross-sectional FE-SEM images (Figure S13 and S14, Supporting Information) before cycling, after initial lithiation, and after initial de-lithiation. Initially, the thickness of graphite blended Si/HNC/AC@Pitch30 was 30.6 μm, which increased by 10.5% to 33.8 μm, and then decreased by 6% to 31.9 μm. Considering that Si particles expand by around 360% during lithiation process, these findings suggest that the unique structure of Si/HNC/AC@Pitch30 composite

microsphere can effectively buffer the volume changes of Si particles, maintaining the structural integrity of the electrode. The overall change of the electrode thickness after the initial activation cycle was 4.2%, which can be considered very low. In comparison, the overall thickness changes for graphite-blended Si/AC@Pitch30, Si/AC, and Si electrodes were 38.0, 48.9, and 83.8% (Table S4, Supporting Information), respectively, clearly highlighting the structural robustness of Si/HNC/AC@Pitch30 microspheres during cycling. Additionally, the cell demonstrated excellent rate performance, delivering discharge capacities of 193, 181, 175, 169, 160, 144, 133, and 107 mA h g^{-1} at 0.1, 0.3, 0.5, 0.7, 1.0, 2.0, 3.0, and 5.0 C, respectively (Figure 7e). These findings highlight the significant potential of the Si/HNC/AC@Pitch30 microspheres for practical energy storage applications when paired with the NCM811 cathode.

Electrochemical impedance spectroscopy (EIS) analysis was conducted to examine the factors contributing to the excellent cycling and rate performance of Si/HNC/AC@Pitch30 microspheres. The Nyquist plots of Si/HNC/AC@Pitch30, Si/AC@Pitch30, and Si/AC microspheres obtained before cycling (denoted as "Fresh") and after 1st, 100th, and 500th cycles are presented in **Figure 8**a–d and are deconvoluted using the Randle-type equivalent circuit depicted in Figure S15 (Supporting Information). Before cycling, since SEI layer was not formed on the electrode, the circuit in Figure S15a
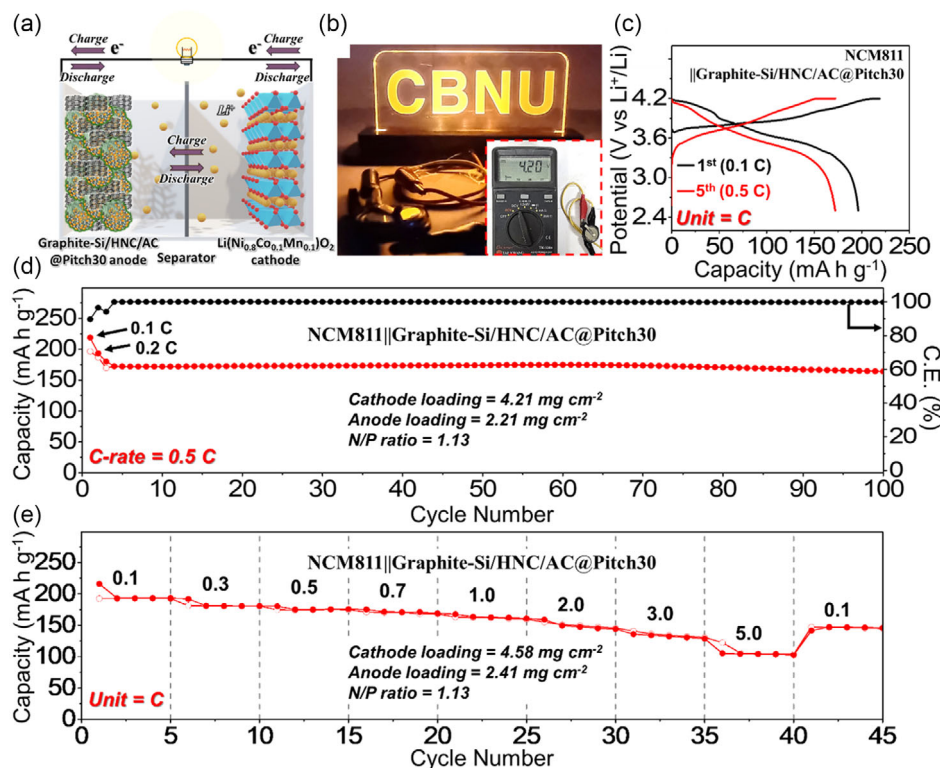
**ADVANCED
SCIENCE NEWS**

www.advancedsciencenews.com

**small
structures**

www.small-structures.com

Figure 7. a) Schematic diagram of full cell consisting of $Li(Ni_{0.8}Co_{0.1}Mn_{0.1})O_2$ (NCM811) cathode and graphite-blended Si/HNC/AC@Pitch30 anode, b) digital image of a light-emitting diode (5 V, 10 mW) powered by one cell utilized after fully charging at 0.1 C (1.0 C = 180 mA g^{-1}), c) initial Galvanostatic charge/discharge voltage profiles at current densities of 0.1 C and 0.5 C, d) cycling performance at 0.5 C, and e) rate capability test.

(Supporting Information) was used to deconvolute Nyquist plots. After many cycles, as shown in Figure 8c,d, the two semicircles can be explicitly differentiated, and therefore the circuit in Figure S15b (Supporting Information) was used to quantify the resistance. In a typical Nyquist plot, the semicircle observed at high and midfrequencies corresponds to the R_f (resistance from SEI-related components) and R_{ct} (charge transfer resistance), respectively. The changes in R_s, which is a bulk electrolyte resistance, and R_{ct} and R_f values as a function of cycle numbers are summarized in Table S5 (Supporting Information). Before cycling, Si/HNC/AC@Pitch30, Si/AC@Pitch30, and Si/AC microspheres exhibited R_{ct} values of 238, 302, and 367 Ω. This finding suggests that coating the surface with pitch-derived carbon coating and compositing Si particles with N-doped carbon derived from ZIF-8 can effectively form 3D conductive matrix, thereby reducing the resistance. After the first cycle, the Nyquist plot shows no distinct separation between R_f and R_{ct} may be because the SEI layer is not fully developed or stabilized. After the first cycle, R_{ct} values were greatly decreased in comparison to before cycling due to the formation of ultrafine nanocrystals during the initial cycle.[61,62] Nyquist plots obtained after the 100th and 500th cycles exhibited two distinct semicircles, where the R_f and R_{ct} values of Si/HNC/AC@Pitch30 were much lower in comparison to Si/AC@Pitch30 and Si/AC microspheres after 500th cycle, indicating the structural robustness of the uniquely structured microspheres. Additionally, electronic and ionic conductivities of Si/HNC/AC@Pitch30, Si/AC@Pitch30, and

Si/AC anodes were measured to provide further insight into the differences observed in electrochemical performance. Resistance (R) values of Si/HNC/AC@Pitch30, Si/AC@Pitch30, and Si/AC microspheres were obtained using a four-point probe method, and electronic conductivity (σ_{e^-}) was subsequently calculated using the formula $\sigma_{e^-} = 1/\rho = L/RA$, where L is the electrode thickness and A is the electrode area (1.5386 cm^2). Considering the electrode thicknesses of 37 μm (Si/HNC/AC@Pitch30), 50 μm (Si/AC@Pitch30), and 35 μm (Si/AC), the measured electronic conductivities were 5.91×10^{-6}, 4.09×10^{-6}, and 0.29×10^{-6} S cm^{-1}, respectively (Table S6, Supporting Information). This indicates that the HNC structure derived from ZIF-8 provides a conductive framework enhancing electron transport, with additional improvements from the pitch-derived carbon coating through enhanced interparticle connectivity and reduced interface resistance. Moreover, ionic conductivities (σ_{Li^+}) were determined from R_{ct} values obtained by EIS measurements, using the formula $\sigma_{Li^+} = L/R_{ct}A$. The electrode thicknesses (L) used for calculation were 45 μm (Si/HNC/AC@Pitch30), 41 μm (Si/AC@Pitch30), and 26 μm (Si/AC). The ionic conductivity values calculated before cycling, after the first cycle, and after the 500th cycle are summarized in Table S7 (Supporting Information). Si/HNC/AC@Pitch30 anode exhibited the highest ionic conductivity during cycling, suggesting that the stable and porous HNC framework facilitates efficient electrolyte penetration and ion diffusion. The increase in ionic conductivity after the initial cycle
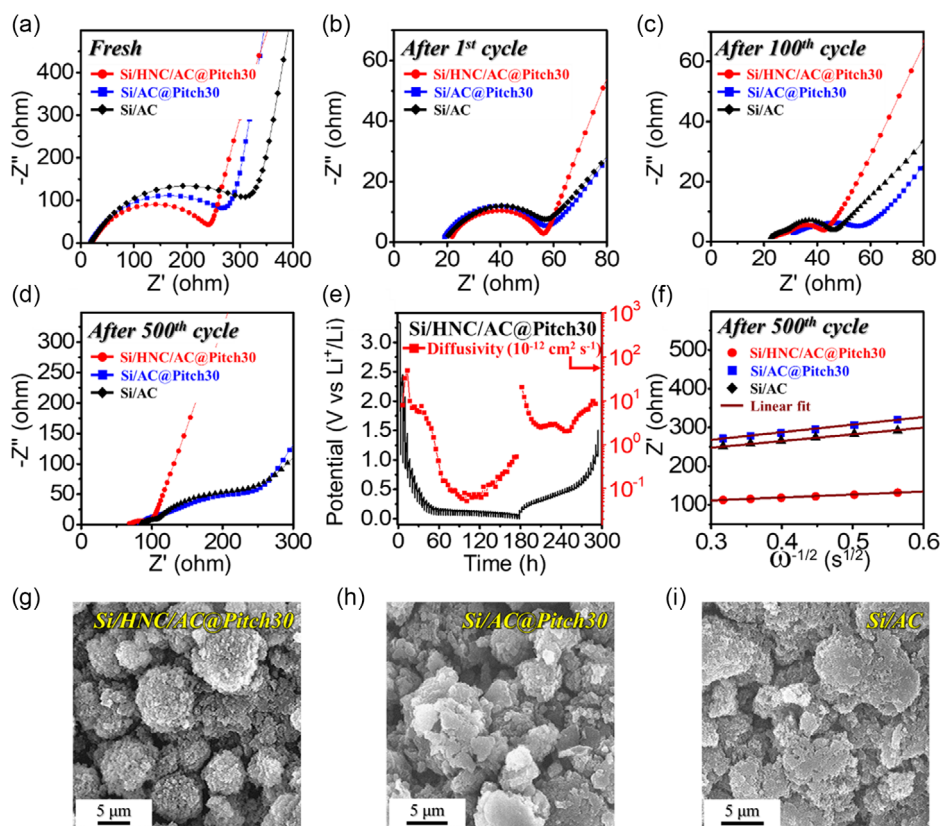
Figure 8. a–d) Nyquist impedance plots of Si/HNC/AC@Pitch30, Si/AC@Pitch30, and Si/AC microspheres: a) before cycling, b) after the first cycle, c) 100th cycle, and d) 500th cycle; e) Li–ion diffusion coefficient (D_{Li^+}) measurements using GITT curve of Si/HNC/AC@Pitch30; f) relationships between the real part of the impedance (Z_{re}) and $\omega^{-1/2}$ obtained after 500 cycles at 1.0 A g^{-1}; and FE-SEM images of the g) Si/HNC/AC@Pitch30, h) Si/AC@Pitch30, and i) Si/AC microspheres obtained after 500 cycles at 1.0 A g^{-1}.

across all samples is attributed to the formation of ultrafine nanocrystalline structures during lithiation/delithiation. In contrast, Si/AC@Pitch30 anode exhibited moderate ionic conductivity initially, which significantly increased after the first cycle but decreased notably after 500 cycles, indicating initial benefits from pitch-derived carbon coating but structural degradation over prolonged cycling. Si/AC anode exhibited the lowest ionic conductivity across all stages, confirming that the absence of both the HNC framework and pitch-derived carbon layer limits ionic transport. To understand the difference in lithium–ion diffusivity among the samples, Galvanostatic intermittent titration techique (GITT) tests were performed for the initial charge and discharge process at a current density of 0.1 A g^{-1}, with a pulse duration of 30 min and a relaxation period of 3 h, where the resulting profiles are shown in Figure 8e, S16a, and S16b (Supporting Information). The lithium–ion diffusion coefficients (D_{Li^+}) values for the anode materials are determined using Fick's second law.[62]

$$D_{Li^+} = \frac{4}{\pi\tau}\left(\frac{m_b V_M}{M_b S}\right)^2\left(\frac{\Delta E_s}{\Delta E_\tau}\right)^2\left(\tau \ll \frac{L^2}{D}\right) \tag{1}$$

where τ is the current pulse time, m_b is the mass of active material, V_M is the molar volume of the active material, M_b is the molecular weight of active material, S is the geometric area of the electrode,

and ΔE_s is the potential change after every equilibrium process. The method for determining ΔE_s and ΔE_τ values is explained in Figure S17 (Supporting Information). The D_{Li^+} values of Si/HNC/AC@Pitch30, Si/AC@Pitch30, and Si/AC microspheres obtained simply by averaging the diffusion coefficients at all potentials were 4.00×10^{-12}, 3.84×10^{-12}, and 4.43×10^{-12} cm^2 s^{-1}, respectively (Table S8, Supporting Information). Ion diffusivity is closely related to the specific surface area and the porosity of the samples, and therefore Si/AC microspheres with the largest BET-specific surface area (242 m^2 g^{-1}) exhibited the largest averaged D_{Li^+} values, although the difference in the values was very tiny among the samples.[63,64] D_{Li^+} can be also calculated from the linear component in the low frequency region of the Nyquist plots using the following equation, where the meaning of the parameters are well-explained in the previous studies.[50]

$$D_{Li^+} = \frac{0.5 R^2 T^2}{A^2 F^4 C^2 \sigma_\omega^2} \tag{2}$$

For the 500th cycle, D_{Li^+} for Si/HNC/AC@Pitch30 was the highest, followed by Si/AC, and then Si/AC@Pitch30 microspheres. The reason for the highest D_{Li^+} for Si/HNC/AC@Pitch30 microspheres may be attributed to the presence of N-doped carbon hollow nanocages derived from ZIF-8

materials, forming 3D conductive channels that can facilitate the ion and electron transportation even after long-term cycling. Si/AC microspheres exhibit much higher specific surface area and larger amount of pore in comparison to Si/AC@Pitch30 microspheres ($242 \, m^2 \, g^{-1}$ vs. $60 \, m^2 \, g^{-1}$), which could facilitate the diffusion of lithium–ions. Therefore, even though pitch carbon with moderate conductivity is coated at the interior and also on the surface, Si/AC microspheres without pitch-derived carbon coating exhibited higher diffusivity due to the highly developed pore structure. To confirm the structural stability of Si/HNC/AC@Pitch30, Si/AC@Pitch30, and Si/AC microspheres, the cells were disassembled after 500 cycles at $1.0 \, A \, g^{-1}$, and their morphologies were observed with FE-SEM (Figure 8g–i). After 500 cycles, the Si/HNC/AC@Pitch30 microsphere (Figure 8g) maintained its spherical shape throughout the structure, even after 500 cycles. This suggests that the internal stress caused by volume changes due to the reaction between lithium ions and Si during long-term cycling can be effectively accommodated by the hollow nitrogen-doped carbon nanocage derived from ZIF-8 and the pitch-derived carbon layer uniformly coated on the surface of the structure. On the other hand, Si/AC@Pitch30 and Si/AC microspheres (Figure 8h,i) were unable to withstand the volume changes of Si, leading to the complete collapse of the structure into aggregated powder. To further substantiate the effectiveness of the carbon-coating design in suppressing silicon volume expansion, atomic force microscopy (AFM) measurements were conducted in force-distance mode to quantitatively evaluate the mechanical properties of the silicon-based anode. The measured average Young's modulus values for Si/HNC/AC and Si/HNC/AC@Pitch30 anodes were 0.7 and 1.0 GPa, respectively (Table S9, Supporting Information). The observed increase in Young's modulus following pitch-derived carbon coating indicates significantly improved mechanical strength and structural rigidity of the anode material. This enhancement can be attributed to structural densification and a reduction in specific surface area imparted by the pitch-derived carbon layer, which consequently provides greater resistance to mechanical deformation under stress. These improvements in mechanical integrity effectively mitigate large volume expansions typically encountered by silicon during lithiation and delithiation, ultimately contributing to enhanced structural stability, minimized crack formation, and improved cycling performance. In addition to mechanical analysis, XPS was conducted on the Si/HNC/AC@Pitch30 anode after 500 cycles at a current density of $1.0 \, A \, g^{-1}$ to investigate changes in surface chemical composition and SEI formation (Figure S18, Supporting Information). The XPS survey spectrum (Figure S18a, Supporting Information) confirms the presence of Li, F, O, C, and Si species, indicating the formation of SEI and the preservation of active silicon. The Li 1s and F 1s spectra (Figure S18b,c, Supporting Information) reveal peaks corresponding to LiF and Li_2CO_3, which originate from the decomposition of carbonate-based electrolytes.[65–67] In particular, LiF is a key decomposition product of fluoroethylene carbonate (FEC) and plays a critical role in forming a robust SEI that suppresses continuous side reactions. The F 1s and Si 2p spectra (Figure S18c,d, Supporting Information) also show the presence of Si–F species, resulting from the reaction of FEC-derived HF with the silicon surface.[67,68] The O 1s and C 1s spectra (Figure S18e,f,

Supporting Information) support the existence of SEI components.[67–69] Additionally, the Si 2p spectrum (Figure S18d, Supporting Information) reveals a distribution of chemical states, including Si^0, Si^{1+}, Si^{2+}, and Si^{3+}, as well as Li_xSiO_y phases, suggesting the coexistence of Si, partially fluorized Si, and irreversible lithiated silicon oxides.[68,69] Notably, the Si^0 $2p_{1/2}$ and $2p_{3/2}$ peaks shift from 100.2 and 99.7 eV (before cycling) to 99.6 and 98.8 eV (after cycling), respectively, indicating amorphization of crystalline Si due to repeated lithiation/delithiation. This amorphization leads to more homogeneous reaction kinetics and improved reversibility. Overall, the XPS analysis demonstrates that the stable SEI layer combined with amorphous silicon structure contributes to the superior long-term electrochemical performance of the Si/HNC/AC@Pitch30 anode.

3. Conclusions

In this work, an innovative approach of preparing microspherical anode consisted of uniformly distributed Si nanoparticles composited with N-doped carbon nanocages derived from ZIF-8 and pitch-derived carbon coating is introduced in detail. After synthesizing ZIF-8 polyhedra with an average diameter of 40–50 nm through a liquid-phase process, they were included in a spray solution along with Si nanoparticles and dextrin for a spray-drying process. Following this, Si/HNC/AC microspheres were synthesized through a subsequent carbonization heat treatment process. A pitch-derived carbon coating process was then introduced to the Si/HNC/AC microspheres, ultimately yielding Si/HNC/AC@Pitch30 microspheres. When tested as half-cell, Si/HNC/AC@Pitch30 microspheres exhibited superior electrochemical performance in comparison to samples prepared without HNCs and without both HNCs and pitch-derived carbon coating. To assess the practicality of the prepared anode, it was blended with commercial graphite and paired with an NCM811 cathode for full-cell electrochemical evaluation, where excellent battery performance was observed. This can be attributed to the 3D superstructure composed of Si nanoparticles distributed within N-doped carbon matrix to which pitch-derived carbon is uniformly coated, which could effectively alleviate the volume changes and provide high electrical conductivity.

4. Experimental Section

Synthesis of ZIF-8 Polyhedra: ZIF-8 was synthesized through a liquid-phase process and used as the forming material to create uniform-sized hollow nitrogen-doped carbon cages within the microspheres. The synthesis process of ZIF-8 followed the method reported in previous studies.[48] First, 19.2 g of 2-methylimidazole (2-methylimidazole, 99.0%, Thermofisher Scientific) was added to 480 mL of methanol (99.8%, SAMCHUN) and continuously stirred. 8.4 g of zinc nitrate hexahydrate ($Zn(NO_3)_2 \cdot 6H_2O$, $M_w = 297.47 \, g \, mol^{-1}$, SAMCHUN) was dissolved in 360 mL of methanol contained in another beaker by stirring continuously. The two solutions were mixed together by slowly adding one solution to the other, and the mixed solution was left at room temperature without stirring for 6 h. The mixture solution was subjected to centrifugation, followed by washing with ethanol (95.0%, DUKSAN) for three times. The resulting material was dried in an oven at 60 °C for 12 h to obtain the ZIF-8 polyhedra.

Synthesis of Si/HNC/AC Microspheres: Si/HNC/AC microspheres were synthesized through a spray-drying process and subsequent heat treatment. First, 1.0 g of ZIF-8 was added to 30 mL of distilled water and ultrasonically dispersed for 6 h. Subsequently, 1.0 g of Si nanopowder was added to the solution, and the solution was stirred for 3 h. Following this, 1.5 g of dextrin hydrate was added, and the mixture was stirred continuously for an additional 12 h. The prepared colloidal solution was then introduced into the spray dryer through a two-fluid nozzle. The flow rate of the solution entering the nozzle was 1.0 mL min^{-1}, and the spraying pressure was maintained at 0.17 bar. The inlet and outlet temperatures of the spray dryer were set to 190 and 100 °C, respectively. The powder obtained from the spray-drying process was placed inside an alumina crucible, and heat treatment was carried out in a furnace with nitrogen (N$_2$) gas flowing at 350 cc min^{-1} The temperature was increased at a rate of 5 °C min^{-1} until 1000 °C was reached, and carbonization was conducted for 2 h.

Synthesis of Si/HNC/AC@Pitch30 Microspheres: The bulk pitch powder was first dissolved in THF to prepare a pitch-THF solution. This solution was then gradually added dropwise onto the Si/HNC/AC microspheres, allowing the powder to absorb the solution. To optimize the pitch-derived carbon coating layer, pitch powder was incorporated into Si/HNC/AC microspheres at weight ratios ranging from 10 to 50% relative to their total combined weight. Since the viscosity of the pitch-THF solution significantly influences the thickness and uniformity of the carbon coating layer, the concentration of pitch in THF was consistently maintained at 25 wt% by proportionally adjusting the amount of THF solvent with increasing pitch content. The resulting slurry was thoroughly mixed using an agate mortar and subsequently dried under ambient air conditions. The dried mixture was then subjected to carbonization at 900 °C for 3 h in a N$_2$ atmosphere, which resulted in the formation of pitch-derived conductive carbon.

Preparation of Si/AC@Pitch30 and Si/AC Microspheres: For preparation of spray drying solution for obtaining Si/AC@Pitch30 microspheres, 1.0 g of Si nanopowder is added to 30 mL of distilled water and stirred for 3 h. Subsequently, 2.0 g of dextrin hydrate is added, and the mixture is further stirred for 12 h to prepare a colloidal solution for spray drying. The amount of dextrin added during the preparation of Si/AC@Pitch30 microspheres is different from that for Si/HNC/AC@Pitch30 so that the amount of carbon in each microsphere remains consistent across the samples. The rest of the preparation procedure is identical to that for Si/HNC/AC@Pitch30 microspheres. For preparation of Si/AC microspheres, all the procedure for preparing spray drying solution remains largely the same, except that the amount of dextrin hydrate added is 3.4 g.

Supporting Information

Supporting Information is available from the Wiley Online Library or from the author.

Acknowledgements

Conflict of Interest

The authors declare no conflict of interest.

Author Contributions

Jae Seob Lee: conceptualization (lead); data curation (lead); software (lead); visualization (lead); writing—original draft (equal). **Geon Hui Oh**: data curation (lead); resources (lead); software (lead); visualization (lead); writing—original draft (equal). **Chungyeon Cho**: data curation (equal); resources (equal); validation (lead). **Noeul Kim**: data curation (equal); software (supporting). **Rakesh Saroha**: data curation (equal); visualization (lead); writing—original draft (equal). **Sang Mun Jeong**: conceptualization (equal); funding acquisition (equal); investigation (equal). **Jae-Oh Shim**: conceptualization (equal); validation (equal). **Dae Soo Jung**: investigation (equal); software (equal). **Gi Dae Park**: investigation (lead); supervision (lead); visualization (equal); writing—original draft (equal). **Yun Chan Kang**: conceptualization (equal); investigation (equal); supervision (equal). **Jin-Sung Park**: software (lead); supervision (equal); visualization (lead); writing—original draft (equal); writing—review & editing (lead). **Jung Sang Cho**: conceptualization (lead); data curation (lead); funding acquisition (lead); supervision (lead); validation (lead); writing—review & editing (lead). **Jae Seob Lee** and **Geon Hui Oh** contributed equally to this work.

Data Availability Statement

Research data are not shared.

Keywords

[1] Y. J. Jo, N. H. Choi, J. D. Lee, *Korean J. Chem. Eng.* **2022**, *39*, 928.

[2] J. Kim, J. Choi, J. Park, H. Son, J. Choi, S. Chae, *Korean J. Chem. Eng.* **2024**, https://doi.org/10.1007/s11814-024-00364-2.

[3] J. S. Lee, R. Saroha, J. H. Oh, C. Cho, B. Jin, D.-W. Kang, J. S. Cho, *J. Ind. Eng. Chem.* **2022**, *114*, 276.

[4] D. Sui, M. Yao, L. Si, K. Yan, J. Shi, J. Wang, C. C. Xu, Y. Zhang, *Carbon* **2023**, *205*, 510.

[5] Q. Zhang, J. Liao, M. Liao, J. Dai, H. Ge, T. Duan, W. Yao, *Appl. Surf. Sci.* **2019**, *473*, 799.

[6] M. A. Azam, N. E. Safie, A. S. Ahmad, N. A. Yuza, N. S. A. Zulkifli, *J. Energy Storage* **2021**, *33*, 102096.

[7] H. Cheng, J. G. Shapter, Y. Li, G. Gao, *J. Energy Chem.* **2021**, *57*, 451.

[8] A. M. Escamilla-Perez, A. Roland, S. Giraud, C. Guiraud, H. Virieux, K. Demoulin, Y. Oudart, N. Louvain, L. Monconduit, *RSC Adv.* **2019**, *9*, 10546.

[9] S. Han, M. Park, S. Huh, Y. S. Won, *Korean J. Chem. Eng.* **2023**, *40*, 1234.

[10] Y. Qiu, C. Zhang, C. Zhang, Q. Xie, Z. Qiao, X. Zeng, W. Xu, H. Zheng, S. Li, J. Lin, D.-L. Peng, *J. Alloy Compd.* **2021**, *877*, 160240.

[11] Y. Song, L. Zuo, S. Chen, J. Wu, H. Hou, L. Wang, *Electrochim. Acta* **2015**, *173*, 588.

[12] Q. Wei, Y. M. Chen, X. J. Hong, C. L. Song, Y. Yang, L. P. Si, M. Zhang, Y. P. Cai, *J. Colloid Interface Sci.* **2020**, *565*, 315.

[13] F. Dou, L. Shi, G. Chen, D. Zhang, *Electrochem. Energy Rev.* **2019**, *2*, 149.

[14] Q. Shi, J. Zhou, S. Ullah, X. Yang, K. Tokarska, B. Trzebicka, H. Q. Ta, M. H. Rümmeli, *Energy Storage Mater.* **2021**, *34*, 735.

[15] Y. Wang, F. Yang, T. Wu, G. Huang, *J. Energy Storage* **2024**, *101*, 113794.

[16] T. Yoon, T. Bok, C. Kim, Y. Na, S. Park, K. S. Kim, *ACS Nano* **2017**, *11*, 4808.

[17] D. Zhang, R. Yang, J. Zhou, W. Liu, H. Qin, Z. Zhang, X. Lei, A. Lu, Z. Mo, L. Miao, F. Dang, *Energy Storage Mater.* **2023**, *63*, 102976.

[18] R. Saroha, J. H. Oh, Y. H. Seon, Y. C. Kang, J. S. Lee, D. W. Jeong, J. S. Cho, *J. Mater. Chem. A* **2021**, *9*, 11651.

[19] W. Bo, C. Li, D. Yang, Y.-Z. Zhang, L. Hu, Q. Gong, J. Zhang, Y. Zhang, M. Li, J. Wei, Y. Zhou, D. Zhou, T. Wu, L.-F. Chen, A. Cabot, *Energy Environ. Sci.* **2025**, *18*, 1929.

[20] Z. Chen, G. Zhang, Q. Hu, Y. Zheng, S. Cao, G. Chen, C. Li, T. Boyko, N. Chen, W. Chen, T. Regier, J. Dynes, J. Wang, H.-T. Wang, J. Zhou, S. Sun, *Small Struct.* **2022**, *3*, 2200031.

[21] L. F. Chen, C. C. Hou, L. Zou, M. Kitta, Q. Xu, *Sci. Bull.* **2021**, *66*, 170.

[22] W. J. Ahn, B. H. Park, S. W. Seo, S. Kim, J. S. Im, *Carbon Lett.* **2023**, *33*, 2349.

[23] M. K. Majeed, R. Iqbal, A. Hussain, M. Lotfi, M. U. Majeed, M. Z. Ashfaq, M. S. Javed, M. Ahmad, A. Saleem, *Sustainable Energy Fuels* **2023**, *7*, 1084.

[24] Q. Wei, Y.-M. Chen, X.-J. Hong, C.-L. Song, Y. Yang, L.-P. Si, M. Zhang, Y.-P. Cai, *Appl. Surf. Sci.* **2020**, *511*, 145609.

[25] K. Chen, Z. Li, J. Zhou, J. Gao, H. Qin, W. Liu, X. Lei, X. Wang, L. Miao, *Appl. Mater. Today* **2025**, *42*, 102561.

[26] Z. Huey, M. C. Schulze, G. M. Carroll, C. Engtrakul, C.-S. Jiang, S. C. DeCaluwe, B. J. Tremolet de Villers, S.-D. Han, *J. Mater. Chem. A* **2024**, *12*, 30465.

[27] B. R. Kim, J. H. Kim, J. S. Im, *Materials* **2022**, *15*, 4713.

[28] N. A. Dunlap, S. Kim, J. J. Jeong, K. H. Oh, S.-H. Lee, *Solid State Ion.* **2018**, *324*, 207.

[29] S. H. Choi, G. Nam, S. Chae, D. Kim, N. Kim, W. S. Kim, J. Ma, J. Sung, S. M. Han, M. Ko, H. W. Lee, J. Cho, *Adv. Energy Mater.* **2018**, *9*, 1803121.

[30] S. Ghosh, U. Bhattacharjee, J. Dutta, K. Sairam, R. Korla, S. K. Martha, *J. Power Sources* **2023**, *584*, 233585.

[31] Z. Chen, J. Wang, J. Lu, C. Ma, X. Liu, J. Wang, W. Qiao, L. Ling, *ACS Appl. Nano Mater.* **2024**, *7*, 6418.

[32] W. He, W. Xu, Z. Li, Z. Hu, J. Yang, G. Qin, W. Teng, T. Zhang, W. Zhang, Z. Sun, X. Yu, *Adv. Sci.* **2025**, *12*, e2407540.

[33] S. Chae, Y. Xu, R. Yi, H. S. Lim, D. Velickovic, X. Li, Q. Li, C. Wang, J. G. Zhang, *Adv. Mater.* **2021**, *33*, e2103095.

[34] F. Wu, Y. Dong, Y. Su, C. Wei, T. Chen, W. Yan, S. Ma, L. Ma, B. Wang, L. Chen, Q. Huang, D. Cao, Y. Lu, M. Wang, L. Wang, G. Tan, J. Wang, N. Li, *Small* **2023**, *19*, e2301301.

[35] S. Liu, Z. Wang, S. Zhou, F. Yu, M. Yu, C. Y. Chiang, W. Zhou, J. Zhao, J. Qiu, *Adv. Mater.* **2017**, *29*, 1700874.

[36] S.-K. Park, J.-S. Park, Y. C. Kang, *Mater. Charact.* **2019**, *151*, 590.

[37] X. Song, Y. Jiang, F. Cheng, J. Earnshaw, J. Na, X. Li, Y. Yamauchi, *Small* **2021**, *17*, e2004142.

[38] R. Saroha, Y. H. Seon, B. Jin, Y. C. Kang, D.-W. Kang, S. M. Jeong, J. S. Cho, *Chem. Eng. J.* **2022**, *446*, 137141.

[39] Y. H. Seon, R. Saroha, J. S. Cho, *Composites, B* **2022**, *237*, 109856.

[40] L. Wu, H. Hou, J. Hu, B. Liu, X. Yang, S. Chen, L. Liu, S. Hu, J. Yang, S. Liang, K. Xiao, S. Yuan, *Micropor. Mesopor. Mater.* **2021**, *317*, 111000.

[41] P. Yadav, T. Bock, Z. Fu, H. Lorenz, I. Gotman, P. Greil, N. Travitzky, *Adv. Eng. Mater.* **2019**, *21*, 1900336.

[42] Y.-C. Hsu, C.-C. Hsieh, W.-R. Liu, *Surf. Coat. Technol.* **2020**, *387*, 125528.

[43] Y. Liu, X. Liu, Y. Zhu, J. Wang, W. Ji, X. Liu, *Energy Fuels* **2023**, *37*, 4624.

[44] Z. Li, H. Zhao, P. Lv, Z. Zhang, Y. Zhang, Z. Du, Y. Teng, L. Zhao, Z. Zhu, *Adv. Funct. Mater.* **2018**, *28*, 1605711.

[45] G. Zheng, Y. Xiang, L. Xu, H. Luo, B. Wang, Y. Liu, X. Han, W. Zhao, S. Chen, H. Chen, Q. Zhang, T. Zhu, Y. Yang, *Adv. Energy Mater.* **2018**, *8*, 1801718.

[46] J. M. Choi, R. Saroha, J. S. Kim, M. R. Jang, J. S. Cho, *J. Power Sources* **2023**, *559*, 232632.

[47] J. S. Lee, J.-S. Park, K. W. Baek, R. Saroha, S. H. Yang, Y. C. Kang, J. S. Cho, *Chem. Eng. J.* **2023**, *456*, 141118.

[48] J. S. Lee, N. Kitchamsetti, J. S. Cho, *Chem. Eng. J.* **2024**, *487*, 150465.

[49] A. Thapa, H. Gao, *J. Electrochem. Soc.* **2024**, *171*, 010504.

[50] J. S. Lee, B. S. Jo, J.-S. Park, J. S. Cho, *Electrochim. Acta* **2025**, *512*, 145440.

[51] A. Nulu, V. Nulu, K. Y. Sohn, *Korean J. Chem. Eng.* **2020**, *37*, 1795.

[52] P. Zhou, L. Pang, Y. Li, H. Fang, P. Xiao, F. Wu, *Carbon* **2024**, *228*, 119389.

[53] B. Deng, L. Shen, Y. Liu, T. Yang, M. Zhang, R. Liu, Z. Huang, M. Fang, X. Wu, *Chin. Chem. Lett.* **2017**, *28*, 2281.

[54] H. Tian, X. Tan, F. Xin, C. Wang, W. Han, *Nano Energy* **2015**, *11*, 490.

[55] X. Zhou, L. Wu, J. Yang, J. Tang, L. Xi, B. Wang, *J. Power Sources* **2016**, *324*, 33.

[56] X. Zhu, S. H. Choi, R. Tao, X. Jia, Y. Lu, *J. Alloy Compd.* **2019**, *791*, 1105.

[57] W. An, B. Gao, S. Mei, B. Xiang, J. Fu, L. Wang, Q. Zhang, P. K. Chu, K. Huo, *Nat. Commun.* **2019**, *10*, 1447.

[58] A. Roland, A. Dupuy, D. Machon, F. Cunin, N. Louvain, B. Fraisse, A. Boucherif, L. Monconduit, *Electrochim. Acta* **2019**, *323*, 134758.

[59] J. Wang, L. Liao, H. R. Lee, F. Shi, W. Huang, J. Zhao, A. Pei, J. Tang, X. Zheng, W. Chen, Y. Cui, *Nano Energy* **2019**, *61*, 404.

[60] R. Guo, X. Liu, B. Wen, F. Liu, J. Meng, P. Wu, J. Wu, Q. Li, L. Mai, *Nano-Micro Lett.* **2020**, *12*, 148.

[61] J. M. Choi, J. S. Lee, J. S. Cho, *Chem. Eng. J.* **2022**, *439*, 135536.

[62] X. Ye, C. Gan, L. Huang, Y. Qiu, Y. Xu, L. Huang, X. Luo, *ChemElectroChem* **2021**, *8*, 1270.

[63] H. Shi, W. Zhang, J. Wang, D. Wang, C. Wang, Z. Xiong, J. Wu, Z. Bai, X. Yan, *Appl. Surf. Sci.* **2023**, *620*, 156843.

[64] X.-K. Wang, J. Shi, L.-W. Mi, Y.-P. Zhai, J.-Y. Zhang, X.-M. Feng, Z.-J. Wu, W.-H. Chen, *Rare Metals* **2020**, *39*, 1053.

[65] G. Jiang, J. Liu, J. He, H. Wang, S. Qi, J. Huang, D. Wu, J. Ma, *Adv. Funct. Mater.* **2023**, *33*, 2214422.

[66] C. Shen, R. Fu, Y. Xia, Z. Liu, *RSC Adv.* **2018**, *8*, 14473.

[67] J. Pereira, L. E. Pichon, R. Dussart, C. Cardinaud, C. Y. Duluard, E. H. Oubensaid, P. Lefaucheux, M. Boufnichel, P. Ranson, *Appl. Phys. Lett.* **2009**, *94*, 071501.

[68] Z.-Y. Wu, L. Deng, J.-T. Li, S. Zanna, A. Seyeux, L. Huang, S.-G. Sun, P. Marcus, J. Światowska, *Batteries* **2022**, *8*, 271.

[69] Q. Wang, M. Zhu, G. Chen, N. Dudko, Y. Li, H. Liu, L. Shi, G. Wu, D. Zhang, *Adv. Mater.* **2022**, *34*, 2109658.